Full Paper

Forging of Hierarchical Multiscale Capabilities for Simulation of Energetic Materials

Brian C. Barnes,*[a] Kenneth W. Leiter,[b] James P. Larentzos,[a] and John K. Brennan[a]

Abstract: We present new capabilities for investigation of microstructure in energetic material response for both explicit large-scale and multiscale simulations. We demonstrate the computational capabilities by studying the effect of porosity on the reactive shock response of a coarse-grain (CG) model of the energetic material cyclotrimethylene trinitramine (RDX), the non-reactive equation of state for a porous representative volume element (RVE) of CG RDX, and utilization of available supercomputing resources for speculative sampling to accelerate hierarchical multiscale simulations. Small amounts of porosity (up to 4%) are shown to have significant effect on the initiation of reactive CG RDX using large-scale reactive dissipative particle dynamics simulations. Non-reactive RVEs are shown to undergo a porosity-dependent pore collapse at hydrostatic conditions, and an existing automation framework is shown to be easily modified for the incorporation of microstructure while retaining reliable convergence properties. A novel predictive sampling method based on use of kernel density estimators is shown to effectively accelerate time-to-solution in a multiscale simulation, scaling with free CPU cores, while making no assumptions about the underlying physics for the data being analyzed. These multidisciplinary studies of distinct yet connected problems combine to provide methodological insights for high-fidelity modeling of reactive systems with microstructure.

Keywords: energetic materials · multiscale simulation · coarse-grain models · dissipative particle dynamics · Gaussian process regression

1 Introduction

Microstructural heterogeneity dictates macroscopic properties and response to thermal and mechanical loading present in most energetic material (EM) applications and technologies. At the grain scale, microstructure can compose various heterogeneities, *e.g.*, voids, defects in and between grains, or species variability, such as mixtures, additives and fillers. Modeling and simulation of EM composites with the entire collection of those explicit heterogeneities is a grand challenge, where an inherent gap in computational capabilities has existed in modeling them with first-principles based models. Simulation of microstructure is challenging due to the disparate spatial and temporal scales over which the phenomena that govern the material behavior occur. For example, material behavior at the mesoscale is linked to the distribution of grain properties (*e.g.*, grain size, orientation, composition), as well as the curvature, interconnectivity, and lattice misorientation of the boundaries between grains. At the atomic scale, the local atomic or molecular arrangement and composition at grain boundaries play important roles in material performance and grain evolution. For EMs, chemical reactivity adds further complexity, as chemical decomposition and energy release primarily occur at the molecular scale, while the explosive effects manifest themselves fully at the continuum scale. Thus, an inherent gap in EM modeling capabilities has existed due to these challenges.

The relentless grind of scientific progress continuously pushes the boundaries of accessible time and length scales in materials simulation through improvements in computer hardware, advancements in algorithms and software engineering, as well as, new methods in physics, materials science, mechanics, and statistical mechanics. In 1998, *Science* published a microsecond-long explicit solvent simulation of protein folding in water [1]. By 2010, a millisecond duration simulation of the same protein was performed using custom hardware [2]. Interestingly, over the same period of 1998 to 2010, the aggregate performance of all supercomputers on the TOP500 list increased by a factor of approximately 1500 times, just slightly outpacing the thousand-fold advance in simulation time scales [3]. At present, nearly 10 years after the first report of that millisecond atomistic simulation, the progress of extending absolute time scales in molecular simulation has slowed down dramatically. Still, a number of exciting developments addressing rare-event problems through accelerated and advanced

[a] *B. C. Barnes, J. P. Larentzos, J. K. Brennan*
Energetic Materials Science Branch, FCDD-RLW-LB
U.S. Army Research Laboratory
Aberdeen Proving Ground, MD 21005-5066
*e-mail: brian.c.barnes11.civ@mail.mil
[b] *K. W. Leiter*
Simulation Sciences Branch, FCDD-RLC-NB
U.S. Army Research Laboratory
Aberdeen Proving Ground, MD 21005-5066

sampling techniques are worth mentioning, including methods capable of leveraging independent multi-microsecond simulations (far too numerous to be reviewed here) [4–7]. Our approach to multiscale method development is also inspired by the desire to more easily treat systems at longer time scales, as the most challenging problems cannot be tackled solely by advancements in computer hardware. The same is true for size scales. The first trillion-atom MD simulation [8] of a simple system was reported in 2008, but a quadrillion-atom simulation remains elusive. Explicit atomistic simulations at macroscale lengths and volumes, incorporating more than 10^{23} particles, do not appear likely in the near future given the state of high-performance computing (HPC) technologies. Thus, atomistic scale simulations of EMs have been mostly limited to idealized microstructures, where modeling of the competing effects of microstructural heterogeneities may not always be possible. The current state of the art for simulation of EMs with first-principles derived models usually involves all-atom reactive molecular dynamics (MD) simulations in order to capture reactivity. Such simulations rely on interatomic potentials that properly describe the energy landscape and transition pathways between the initial material, reaction products, and the relevant transition structures. Many atomic-scale reactive potentials are available (see reviews in [9,10]), with ReaxFF [11,12] likely the most widely used model. For example, all-atom reactive MD simulations of EMs have enabled direct study of the initiation and growth of hotspots (localized high temperature regions that can be further fed energy through exothermic chemical reactivity) in the vicinity of a single microstructural heterogeneity [13]. These simulations, involving only a nanometer sized heterogeneity, still have required the use of petascale computational resources.

Particle-based microscale simulation methods using coarse-grain (CG) models currently offer a promising route for extending the power of atomistic modeling toward the micro- and mesoscale. CG models are developed by grouping a set of smaller entities (*e.g.*, atoms or molecules) into a single larger entity, defined as the CG model. The computational speedup arises from the mapping of the atomistic degrees-of-freedom (d.o.f.) into a reduced set of CG d.o.f. with short-ranged interactions. However, features lost during this coarse-graining process may not be adequately recovered unless correctly reintroduced through an appropriate CG methodology. For instance, as a direct consequence of losing molecular d.o.f. during coarse graining, use of MD equations of motions with a CG model is inadequate due to effects on the dynamics of the CG models (*i.e.*, faster transport behavior) compared to their atomistic counterparts [14]. Furthermore, at the atomistic scale, the formation and breaking of chemical bonds is treated explicitly and is conceptually intuitive; in contrast, CG models must collectively capture and recover the relevant chemical features lost during coarse-graining. While CG models cannot be expected to replicate the full fidelity of

atomistic models, they can produce results of sufficient accuracy across a much broader range of material properties and conditions, and at considerably less computational cost if proper care is taken in recovering the d.o.f. that would otherwise be lost.

Computational capabilities necessary to represent the salient physical and chemical features of polycrystalline energetic materials through CG particle approaches have recently emerged within the dissipative particle dynamics (DPD) framework [14,15]. These DPD formulations treat reactivity implicitly, and while explicit reactivity methods also exist, they are restricted to isothermal conditions. Explicit simulation within the DPD framework is akin to atomistic-level reactive force-fields (*e.g.*, ReaxFF [11]), which involves explicit bond-breaking and formation, either in a stochastic [16–20] or deterministic fashion [16,19]. An alternative particle-based CG methodology for EM simulation, termed dynamics with implicit degrees of freedom (DID), treats chemical reactivity through a reactive potential [21–25].

Implicit simulation of chemical reactivity using the DPD method (DPD-RX) treats the CG particles as interacting *continuous-stirred tank reactors* [26]. As the chemistry of a CG particle changes, so does its interaction potential so as to correctly capture both heat exchange and pressure-volume work due to chemical reactivity. The DPD-RX approach has been applied to the shock-to-detonation transition (SDT) of liquid nitromethane [15,27], the shock response of TATB [28], and the thermal and mechanical response of RDX [14,29].

CG models used in the DPD-RX formulation can be developed from atomistic models through various coarse-graining techniques. Presently, the most rigorous approaches for developing CG models tend to proceed in a bottom-up fashion, where groups of atoms are mapped into a statistically-equivalent ensemble of structure-less CG particles. A CG potential is then derived via a thermodynamically consistent procedure based upon microscopic statistics [29–34]. These bottom-up methods can be categorized into structure-matching [35], force-matching [36–42], or entropy-matching approaches [43]. For developing CG models of EMs using these approaches [44], atomistic models that reasonably predict experimental properties are available for the most common energetics. The reader is referred to the reviews by Rice and Sewell [45], and more recently by Taylor and Rice [46], which describe the development of EMs both empirically derived and quantum mechanically derived. CG models of EMs have been derived from non-reactive classical potentials, rather than reactive potentials, since chemical reactivity is modeled in the unique CG manner described below.

While there are specific problem classes that are well-suited for discrete particle simulations at these scales, there remains much work to be done to extend accessible length and time scales in order to investigate SDT for weaker shocks, sub-detonative response of materials or slow cook-off problems. This highlights areas of opportunity where

continued development of micro- and meso-scale models can provide insight to the initiation mechanisms that would otherwise not be captured through atomistic-scale simulations. To this end, multiscale approaches that can couple the CG methods with the continuum length and time scales are attractive to be able to fully examine SDT or slow cook-off problems, and make at-scale comparisons with experimental measurements [47].

Through a variety of multiscale approaches, researchers seek to bypass limits faced by discrete particle simulations [48–54]. This is critically important for energetic materials so that continuum simulations can incorporate the effects of microscale or mesoscale structural features in materials, while using information that is ultimately sourced from quantum mechanical simulations. Such an approach is in contrast to continuum material models that are typically empirically parameterized against experiment. Thus, there is interest in scale-bridging information from lower length- and time-scale simulations to inform models at the continuum scale. Recently, atomistic simulations have been used to parameterize continuum energetic material models for plasticity during pore collapse [55], elastodamage [56], equations of state [57,58], ignition [59], and both nonlinear elasticity and phase transformation [60]. Accurate first-principles modeling and simulation is invaluable for the parameterization of models where experimental data is scarce or entirely unavailable, and thus may be especially useful in predictions of macroscale properties for materials that are not easily available *en masse.* EMs are often dangerous to synthesize or transport and thus are a target for first-principles modeling.

Efforts to incorporate microstructure in EM continuum simulations have largely been motivated by the need for more physically detailed simulations of ignition and initiation. Two-dimensional (2-d) plane-strain simulations of impact on systems with pores [13,61,62] or grains [63,64] are popular model systems for continuum studies. Another approach to microstructure-dependent multiscale response is the use of detailed mesoscale continuum simulations to inform continuum response [65–68]. In the future, detailed simulations at the mesoscale level may be linked to a probabilistic continuum model for ignition or initiation; such probabilistic models appear to be a promising path forward [69]. The approach used in our work is rooted in the Heterogeneous Multiscale Method [70,71] (HMM) as implemented for a Hierarchical Multiscale Simulation (HMS) of an energetic material [72–75]. The HMM approach has also been used for coupling of atomistic simulations to continuum simulation for other materials, such as metals [76–79]. Application of HMM to a particular problem relies on careful specification of the information provided to, and required from, the microscale simulation, which in this work will be the equation of state (EOS) response for an energetic material. The HMM framework relies on the microscale model having a form that is consistent with the macroscale variables and problem structure; thus, the

microscale solver is given macroscale variables as input, may have constraints based on the form of the macroscale problem and its conservation laws, and in turn provides estimates of required missing macroscale variables. As the complexity of the multiscale problem increases, such as the presence of microstructure within the materials, the complexity of the microscale solver (or set of solvers) may also increase. These solvers may be exceptionally computationally demanding, but that expense can be mitigated through the active learning of a surrogate model, for example, a Gaussian process regression model [80]. Spatially adaptive surrogate model construction has also been performed on-the-fly, in a locally predictive manner [81]. Most HMM efforts to date have involved either computationally inexpensive microscale models or low-dimensional problems. Future multiscale efforts must be capable of routinely tackling computationally demanding microscale models with high-dimensional inputs and outputs, with those inputs possibly serving as evolving parameters of property probability distributions describing the underlying microscale state, as would be needed for some stochastic continuum models. In the case of probability distributions describing the microscale, one can imagine performing stochastic macroscale simulations that require many replicas of microscale simulation to statistically sample the response. The computational requirements and realism of the microscale model are bounded only by nature itself, and thus efficient learning approaches for surrogate models will be needed to perform that type of high-fidelity macroscale simulation on future exascale supercomputers. Reductions in core-hour expense or wall-clock time via use of surrogate models and predictive microscale calculations will enable the use of HMM approaches on a significantly wider range of problems, such as the aforementioned complex microstructures or distributions of material properties at the microscale.

In this paper, we demonstrate progress on a long-term multiscale effort to directly use particle-based microscale models for constitutive evaluations in continuum finite element simulations. Section 2.1 will demonstrate progress at the CG scale for reactive shock simulation of energetic materials with porous microstructure. Section 2.2 will demonstrate that this CG model and porosity can be incorporated into a representative volume element (RVE) for EOS response. Section 2.3 will demonstrate a novel way to use the RVE for speculative sampling of states in an HMS implementation, allowing for the efficient use of computational resources available to a large multiscale simulation. Each section of this paper addresses an independent problem, but the advances in one section are utilized in the design of the multiscale research in the successive section. Collectively, this work shows a path forward to microstructured, macroscale continuum simulations of material models ultimately based on *ab initio* atomistic simulations.
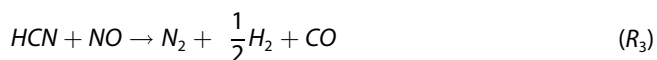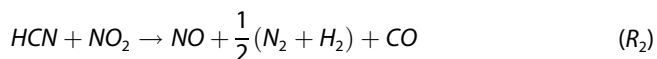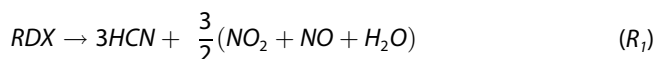
2 Results

2.1 Large-scale DPD-RX Shock Simulations of Coarse-Grain RDX

In this section, we model the shock response of defect-free and porous EMs using discrete particle models. Validation of the shock response in our CG model will allow for reliable construction of CG RVEs that also incorporate microstructure, and guide the selection of salient features to incorporate in those RVEs. We have previously developed CG models of EMs through a force-matching approach, and have successfully modeled the structural as well as the thermodynamic behavior of the materials. Here, we extend our capabilities to simulate the shock response of RDX, a prototypical EM, with the goal of understanding the dependence of the material characteristics on performance under these conditions.

2.1.1 Models and Methods

Particle-based, DPD methods using CG models are applied to simulate 1-d planar shock experiments at the microscale. An energy-conserving DPD variant (DPD-E) [82,83] that was previously extended to include a microscale description of chemical reactivity (DPD-RX) [14,15,27] is applied to model the chemical decomposition, energy release and shock response within porous RDX samples.

In the DPD-RX approach, the CG particles are modeled by treating them as microreactors [14], where an additional equation of motion describing the temporal behavior of a reaction progress variable associated with each CG particle is specified. The DPD-RX scheme does not explicitly depict bond breaking or forming as a reactive potential does. Rather, the chemical identity of the CG particle (reflected through a particle EOS and a typical interaction potential) dynamically evolves through time-dependent changes in the reaction progress variable. The chemical identity of the particles vary from pure RDX to a mixture of small molecule product gases, and states in between, as described by the following 4-step decomposition reaction rate model:

$$RDX \rightarrow 3HCN + \frac{3}{2}(NO_2 + NO + H_2O) \qquad (R_1)$$

$$HCN + NO_2 \rightarrow NO + \frac{1}{2}(N_2 + H_2) + CO \qquad (R_2)$$

$$HCN + NO \rightarrow N_2 + \frac{1}{2}H_2 + CO \qquad (R_3)$$

$$NO + CO \rightarrow \frac{1}{2}N_2 + CO_2 \qquad (R_4)$$

Rate laws are assumed to follow the molecularity of reactions R_1–R_4, where Arrhenius-type reaction rate constants depend on the temperatures of the microreactors (*i.e.*, the particle internal temperatures).

The internal state of a CG particle is described through the CG equation of state (CG-EOS) model, which relates the particle internal temperature to the particle internal energy. The particle internal energy is composed of three contributions that correspond to the mechanical work done on the system, the heat conduction between particles, and the chemical energy released/absorbed by a given particle. Any change in the CG particle chemistry is reflected through a partition function-based CG-EOS.

The CG interaction potential model accounts for changes in the particle chemical character from pure RDX to the product gas mixture (PGM), and states in between. A previously developed CG model for RDX that was up-scaled from quantum-based models through the multiscale coarse-graining (MS-CG) force-matching approach [41,42,44] is applied, where each 21-atom RDX molecule is represented by a single coarse-grain RDX (CG RDX) particle. As RDX decomposes into the product gas species shown in Reaction R_1–R_4, the interaction model accounts for these changes in composition. A full description of the energy conserving DPD-RX method, model, and parameters is given elsewhere [14,29,84].

Simulating at the microscale requires scalable software that can fully utilize HPC resources. The DPD-RX method has been implemented within the LAMMPS simulation software [85–87] under the USER-DPD add-on package. Several features within the USER-DPD package are used in this work, which include the non-reactive energy and enthalpy-conserving DPD variants (DPD-E and DPD-H, respectively) [88], the Shardlow splitting algorithm (SSA) for numerical integration [86,89], the concentration-dependent interaction potentials, and efficient reaction kinetics solvers [90,91] with adaptive time stepping.

2.1.2 Computational Details

In the EM composite models considered here, microstructural heterogeneities are introduced into the samples by creating model geometries containing porosity. Laboratory characterization studies of RDX Comp A-3 (type II) samples report porosities ranging from 0.004% to 0.115%, with inclusions that are 0.1–10 µm in size [47]. Modeling of these porosities and pore sizes in this range requires extremely large model geometries and long simulation times, which would require advanced multiscale techniques that couple the CG models with continuum models, such as the HMS approach [29] discussed in this work. For the results described here, pore sizes of 5 nm are considered at porosities of 0.0%, 2.0% and 4.0%. While additional simulations with fewer, but larger pores and porosities that are closer to the laboratory experiments could be simulated at the CG

scales, our intent in this work is merely to demonstrate the role of porosity on material performance.

Porous RDX samples are constructed by distributing cylindrical pores into a 25 μm × 20 nm × 5 nm single-crystal RDX with density of 1.827 g/cm^3 (1.801 g/cm^3 after equilibration). All cylindrical pores are oriented along the z-axis of the samples, resulting in infinitely long cylinders when applying periodic boundary conditions. For the current study, the pore volumes are not permitted to overlap. To enforce this condition, the positions of the cylindrical pore centers are determined by partitioning the x-domain of the sample into N_{pore} equally-sized subdomain volumes, where each subdomain volume contains the entire volume of exactly one pore that is randomly positioned. The subdomains were sufficiently large to maintain the structural integrity of the pore during equilibration. A total of three RDX sample geometries were constructed, and are summarized in Table 1.

Each of the RDX samples are simulated under shock conditions to examine the influence of microstructure on the material response. Prior to flyer-plate impact with the sample surface, the 3-d periodic samples are equilibrated through a simulation protocol that consists of a 100 ps enthalpy-conserving DPD [88] simulation (using a Nosé-Hoover barostat damping parameter of 10 ps), followed by a 50 ps energy-conserving DPD simulation. After thermalizing the samples to ambient conditions, the boundary conditions are modified to be 2-d periodic in the y- and z-directions, while creating a free surface in the x-direction. A flyer-plate setup is used, where a flat wall interacts with the particles through a Lennard-Jones 9–3 potential with an energy parameter of $\varepsilon = 0.01$ eV, a size parameter of $\sigma = 5.0$ Å, and a cutoff radius $R_{cut} = 12.5$ Å for the wall-particle interaction. The flyer-plate impacts the free surface of the material and maintains a constant velocity, generating a supported shock that interacts with the pores as well as secondary shockwaves generated from those defects, transferring energy to surrounding particles, and locally initiating chemical reactions. The sample materials were chosen to be 25 μm in length, allowing the shockwave to propagate for up to 7 ns before reaching the end of the sample (the impact velocities considered are 2.25 km/s, 2.5 km/s and 3.0 km/s). In total, nanosecond time-scale simulations using a 5 fs time step for the porous samples and a 10 fs time step for the defect-free samples are conducted to model the equilibration and shock wave propagation through the samples. Configurational snapshots of the system states are recorded every 50 ps of simulated time. Also, spatially-distributed histograms of various particle state variables are recorded every 5 ps to collect simulation results at a higher temporal resolution.

2.1.3 Results

We begin by examining the shock response in a perfect RDX crystal to establish the baseline performance of the CG RDX model, and follow with the porous samples to demonstrate the influence of microstructure.

The perfect, defect-free RDX samples are impacted with flyer-plate speeds of 2.25 km/s and 2.5 km/s, propagating a compressive shockwave through the sample at measured shock speeds of ~6.8 km/s and ~7.4 km/s, respectively. At these shock speeds, chemical reactions are observed at the flyer-plate/sample interface immediately after impact. As the RDX decomposition progresses along the reaction pathway, intermediate and product gas species are produced while exothermically releasing energy. Energy is transferred to neighboring particles via heat conduction, while P-V work is done on the neighboring particles as a result of the expanding product gases. Provided that there is sufficient thermal energy transferred to the neighboring particles, the reaction volume will continue to grow as more RDX decomposes. Ultimately, there is a tradeoff between the rate at which energy is generated from the exothermic reactions and the rate at which it is dissipated through the material that will dictate whether the reaction volume growth will persist or terminate.

A convenient way to examine the shock response is by plotting a heatmap of the simulation time versus run distance (coloring by properties such as pressure, temperature, extent of reaction, shock speed, *etc.*) at various shock speeds. In Figure 1, heatmaps of pressure and extent of RDX decomposition are shown for the defect-free RDX crystals impacted with flyer-plate speeds of 2.25 km/s and 2.5 km/s. The shocks are sustained throughout the duration of the simulation, as indicated by the shrinking sample length (*i.e.*, growing white space) shown in Figure 1. For the weaker shock propagating at a speed of ~6.8 km/s, the pressure map (top left frame) shows two distinct regions that illustrate the location of the shock front during the simulation. The unshocked material is initially at a pressure of 0.0001 GPa and rises to a pressure of ~20 GPa in the shocked state. Reactions are observed initially at the flyer-plate/sample interface, but do not progress to form a sustainable reaction wave over the time scales of the simulation (top right frame).

For the stronger shock propagating at a speed of ~7.4 km/s, the pressure map shows two pressure regimes within the 0.0 to ~0.5 ns time frame. At ~0.5 ns, a sudden pressure increase is observed at the flyer-plate/sample interface, which creates a self-propagating reaction wave through the shocked material. The pressure increase is due to the reactions progressing further along the reaction

Table 1. Porous RDX sample geometries.

Sample Size (nm^3)	Porosity (%)	Pore Radius (nm)	N° of Pores
25000 × 20 × 5	0	–	0
25000 × 20 × 5	2	5	124
25000 × 20 × 5	4	5	249
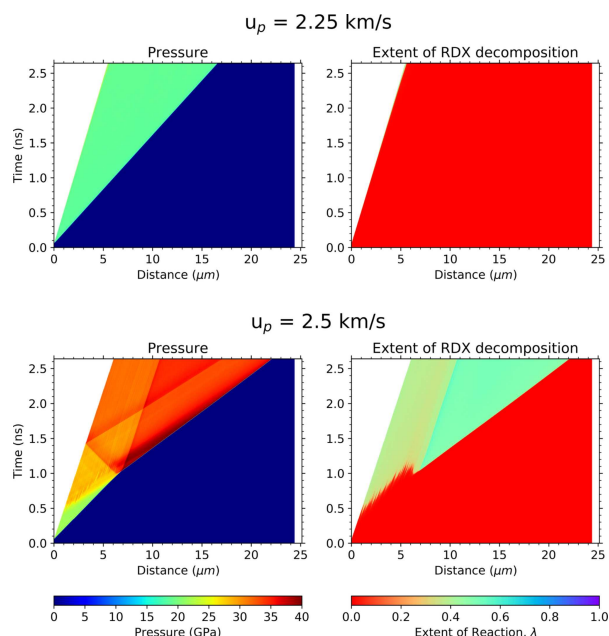
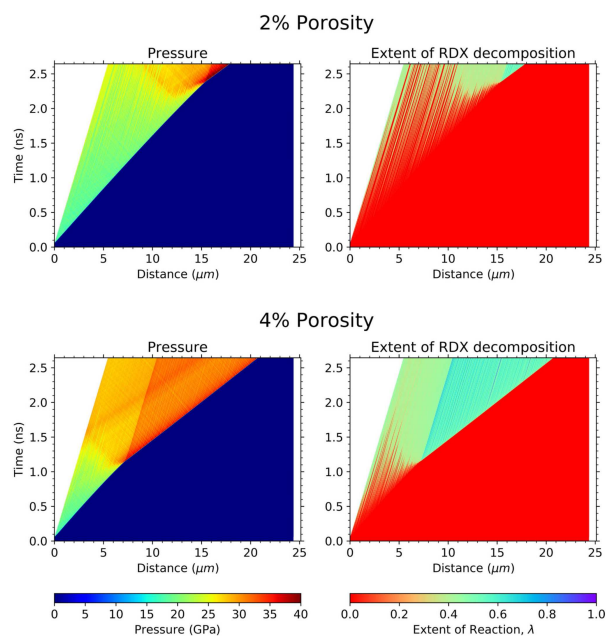*B. C. Barnes, K. W. Leiter, J. P. Larentzos, J. K. Brennan*

Figure 1. Heatmaps of pressure (left frames) and extent of RDX decomposition (right frames) resulting from flyer-plate impact speeds of $u_p = 2.25$ km/s (top frames) and $u_p = 2.5$ km/s (bottom frames) propagating a sustained shock wave through perfect, defect-free RDX samples. The flyer-plate moves at a constant velocity for the duration of the simulation (*i.e.*, white space on the left side of the plots are indicative of regions where no material is present).

Figure 2. Heatmaps of pressure (left frames) and extent of RDX decomposition (right frames) resulting from a shock wave of strength $u_p = 2.25$ km/s propagating through RDX samples with 2% (top frames) and 4% porosity (bottom frames). The white space on the plots indicate that no material is present at those distances.

pathway, producing hot, expanding product gases (see extent of RDX reaction heatmap, bottom right frame). The reaction wave propagates faster than the shock wave, and eventually the waves converge at a run distance of ~7 μm. An additional simulation was conducted at an impact speed of 3.0 km/s. In this case, the reaction wave and shock wave propagate together upon impact, indicating a prompt steady-state reaction wave.

The porous RDX samples are impacted with a flyer-plate speed of 2.25 km/s. Similar to the defect-free samples, chemical reactions are observed at the flyer-plate/sample interface immediately after impact. As the compressive shockwave propagates through the material and encounters a pore, particles at the pore interface are ejected across the pore, colliding with particles on the opposite side of the pore and transferring kinetic energy to those particle's internal degrees-of-freedom. Provided sufficient thermal energy is present within the collapsed pore volume, RDX decomposition is initiated, creating localized hot-spots within the material. Analogous to the defect-free case, with ample energy production rates, the reaction volumes will continue to grow and expand, propagating a reaction wave through the shocked material. The pressure and RDX extent-of-reaction heatmaps for the 2% and 4% porous RDX samples (5 nm voids) at an impact speed of 2.25 km/s are shown in Figure 2. In comparison to the defect-free sample (shown in the top frames of Figure 1), the effect of microstructure is

evident. At an impact speed of 2.25 km/s, the reaction wave and shock wave converges in the porous sample, but does not in the defect-free sample. Close inspection of the RDX extent of reaction heatmap in Figure 2 illustrates the microstructural features, where at early simulation times, the individual reaction volumes resulting from pore collapse appear on the heatmap as long, thin bands of light green lines that eventually combine together at longer simulation times. This is indicative of the reaction volumes coalescing, which may eventually lead to self-propagating reaction wave at longer simulation times.

2.2 Implementation and EOS Results for a Non-Reactive Porosity Model in LIME

In order to investigate the behavior of porous RDX at time and length scales accessible to multiscale models, it is necessary to incorporate porosity into a RVE that can be used within a HMS model of RDX. We have previously demonstrated use of a non-reactive CG RDX model within the HMS framework, where the hydrostatic component of the equation of state (pressure) and temperature response was provided in the finite element simulation [72,73], and those constraints and responses will also be used in this work. In the prior work, the material considered was a perfectly crystalline, defect-free RDX sample. This multiscale coupling was accomplished, in part, through automation of CG RDX

simulations using a module we developed, named the LAMMPS Integrated Materials Engine (LIME) [73]. The heuristics, performance, accuracy and source code for LIME have been described in detail in that work. LIME uses constant-volume DPD-E simulations to collect data for EOS response, and both DPD-E simulations and enthalpy-conserving DPD-H simulations for equilibration before production data collection. Herein, we have extended LIME to support porosity in its simulation cell, also referred to as a RVE. Thus, we create the essential capability to scale both system and void size, as necessary, to provide the non-reactive hydrostatic LIME RVE counterpart to the microstructure-dependent results in section 2.1. The porosity present in the RVE must be specified by the macroscale model before instantiation in LIME.

In this work, the RVE porosity is instantiated by deleting a number of nearest-neighbor shells from the RVE simulation cell. We exploit the fact that our CG RDX model crystal lattice has hexagonal close-packed (hcp) symmetry at ambient conditions, and that we can control the number of unit cell replicas when instantiating our RVE. By specifying both the number of hcp nearest-neighbor shells to delete (beginning at a consistent origin particle) and the size of the RVE, we may carefully control the extent of particles removed. In practice, we use the hcp basis vectors to determine the distance from an origin particle to the Nth shell, and then delete all particles within that radius. This procedure creates a spherical pore. We are able to determine the exact porosity actually present in the RVE by comparing the number of particles before and after the deletion operation. This allows for two exact and independent controls to create pores of differing sizes for systems of the same porosity, thus allowing us to study pore size effects, the results of which will be presented below. After creating a pore in the RVE, the system size must be rescaled. This is because one of the required inputs to LIME is the overall system (RVE) density. By removing particles during pore creation, the system density is lowered. Thus, the rescaling (compression) ensures the RVE density matches the macroscale input density after pore creation. The burden for correct specification of density and porosity falls on the macroscale model, as it is providing the inputs to LIME. For example, if a macroscale model was attempting to simulate a material with an ambient theoretical maximum density (TMD) of 1.8 g/cm^3 and a porosity of 3%, with the only difference of its density from TMD being due to that porosity, then the input to LIME should be a porosity of 3% and density of 1.746 g/cm^3. Creation of the pore occurs before equilibration of the system, and the remaining algorithms and heuristics used in LIME are almost entirely unchanged. The time step used was 5 fs, instead of 10 fs in original LIME, and the number of steps required for any LIME equilibration stage is correspondingly doubled to keep the simulation time constant. Inclusion of a pore in LIME allows for viscoplastic pore collapse to occur, and the subsequent EOS response may therefore include RDX lacking any long-range

order. However, there is no directional shock currently implemented in LIME, and thus hydrodynamic pore collapse cannot be observed. This is consistent with its original design goal of providing hydrostatic information.

In Figure 3, we present the porosity of the system as a heatmap, with a measure of the system size plotted against the number of hcp shells removed for void formation. The reference state is at 1.8 g/cm^3 and defined as zero total internal energy (corresponding to ambient conditions for our CG RDX model). Each individual result in the heatmap is from a different simulation, but each is constrained such that the total energy is 0.0 J/m^3 and at a total system density of 1.8 g/cm^3. Thus, when a larger void is created (proceeding to the right of the map in any given row), the initial density of the surrounding crystalline lattice must increase. Grey data indicates no result and is common at the unphysically high porosities near the bottom right of Figure 3. This may be directly compared to EOS results for pressure in Figure 4 and temperature in Figure 5. Let us consider Figure 4 in greater detail. In the bottom row of data in Figure 4 (# of directional replicas = 14), for simulations where voids remain mechanically stable, the pressure initially increases as void size increases. The pressure increase is due to the crystal lattice density increase from a void size (# removed hcp shells) of zero to eighty in the bottom row of Figure 4. Past that void size, the system cannot be equilibrated with an intact void, and the void collapses, which also has the result of relieving crystal lattice stress and lowering overall system pressure. Comparing Figure 4 and Figure 5, we see that the majority of the temperature increase occurs after peak pressure, when plastic response has occurred. Figure 6 shows the same data as Figure 4, but with porosity as the x-axis and results for different system sizes overlaid (with data points colored by system size, darker shades corresponding to smaller systems). As clearly shown in Figure 6, porosity itself is the
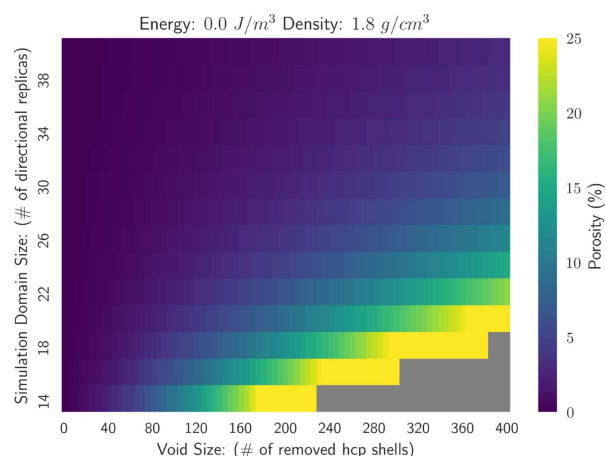
Figure 3. Heatmap of porosity as a function of simulation domain size (# of replicas in one dimension) and void size (# of removed hcp shells) for a reference state at ambient conditions.
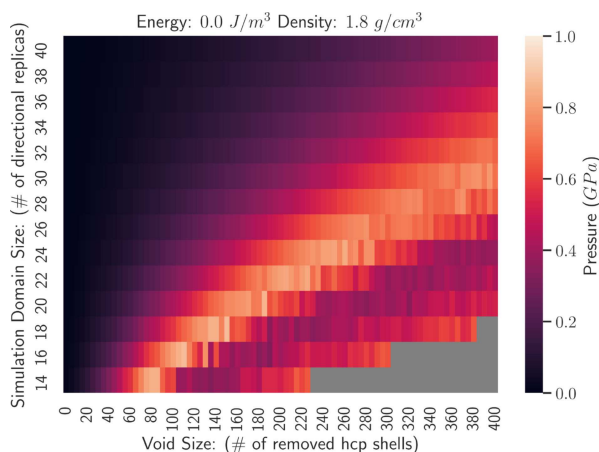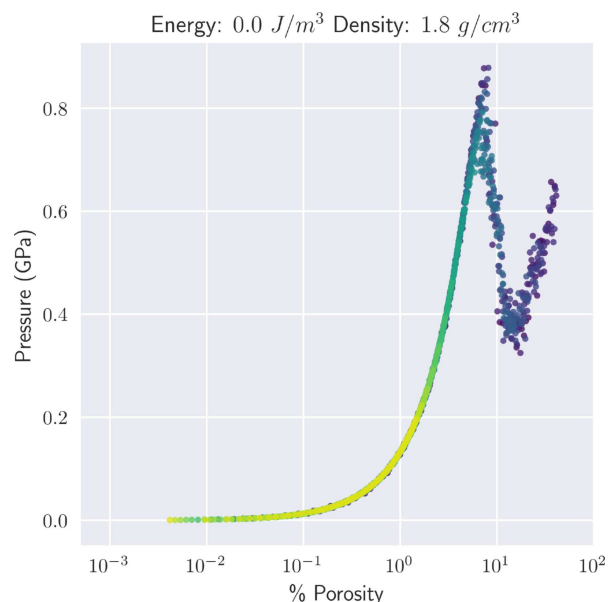
Figure 4. Heatmap of pressure as a function of simulation domain size (# of replicas in one dimension) and void size (# of removed hcp shells) for a reference state at ambient conditions.
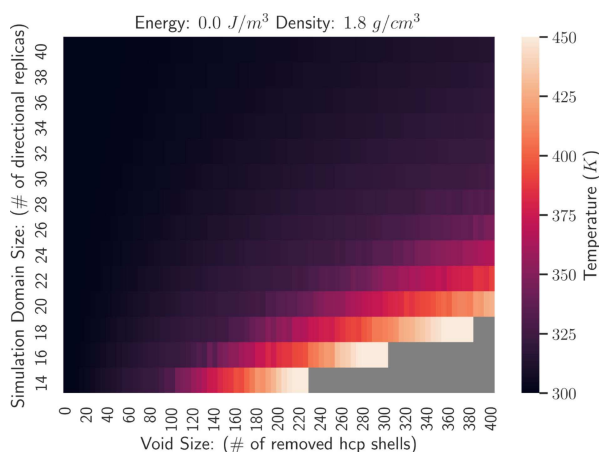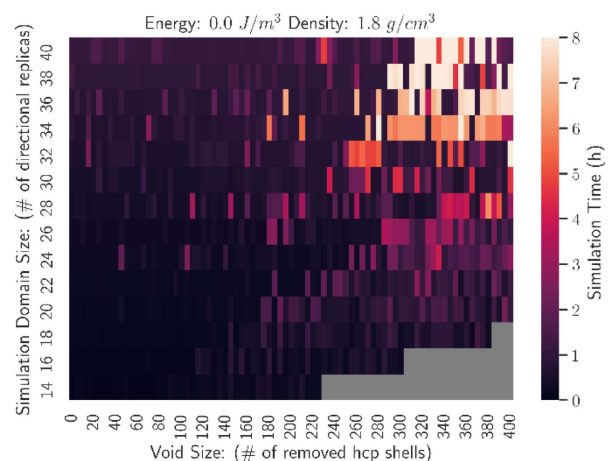

Figure 5. Heatmap of temperature as a function of simulation domain size (# of replicas in one dimension) and void size (# of removed hcp shells) for a reference state at ambient conditions.


Figure 6. Pressure as a function of porosity, with individual data points colored by simulation cell size; this is a different visualization of the data in Figure 4.

Figure 7. Heatmap of total wall-clock time required for LIME to complete as a function of simulation domain size (# of replicas in one dimension) and void size (# of removed hcp shells) for a reference state at ambient conditions.

controlling factor in void collapse for this reference state, with the system providing elastic response up to approximately 9% porosity. While it is unlikely that extremely high porosities will be needed for our applications, we demonstrate the ability of LIME to converge a disordered RVE at those extremes (beyond ~25%). Beyond that point, there is plastic deformation to relieve stress on the lattice and the original void no longer exists.

LIME computational evaluation timings given a constant number of 64 CPU cores are also available, and shown in Figure 7. Large systems that have large pores may take hours to equilibrate, which indicates a need for further development of LIME heuristics as microstructural features are added. However, for small systems of any porosity, equilibration is still relatively rapid.

The results for an ambient reference condition may be contrasted with states of differing density and energy, as may be encountered during a continuum impact simulation. At the high end, in Figure 8, we show pressure response with a simulation cell density of 2.3 g/cm³. This data covers a smaller range of void sizes, as large sizes would lead to completely unphysical densities in the CG RDX lattice surrounding the void. Interestingly, this shows the small void essentially being 'locked in' by the surrounding extremely dense lattice, without a clear void collapse front on the heatmap. The pressure response for a low density

Forging of Hierarchical Multiscale Capabilities for Simulation of Energetic Materials
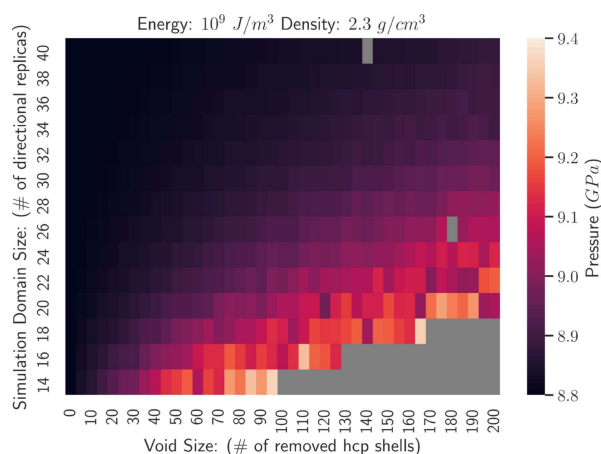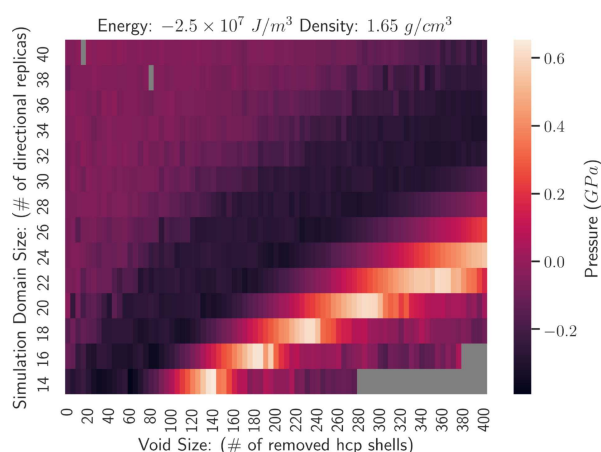

Figure 8. Heatmap of pressure as a function of simulation domain size (# of replicas in one dimension) and void size (# of removed hcp shells) for a high-density reference state.

system is shown in Figure 9, and displays a complex response. As the void size increases, RVE pressure initially decreases (with lattice density approaching ambient solid crystal density). After void size is increased further, the system response resembles that of the reference response, with pressure increasing before a void collapse occurs and releases stress. It should be emphasized that each individual state point is calculated independently at fixed total density and energy, and thus our individual heatmap results do not prescribe a particular physical path the system would take in a dynamic experiment.

Finally, to provide a physical picture of void-containing RVEs at the end of a LIME simulation, a lattice analysis is provided in Figure 10 and Figure 11. As the RVE is that of a solid system, after the pore collapse there may be complex phases (mixture of order and disorder) instead of a homo-

Figure 9. Heatmap of pressure as a function of simulation domain size (# of replicas in one dimension) and void size (# of removed hcp shells) for a low-density reference state.
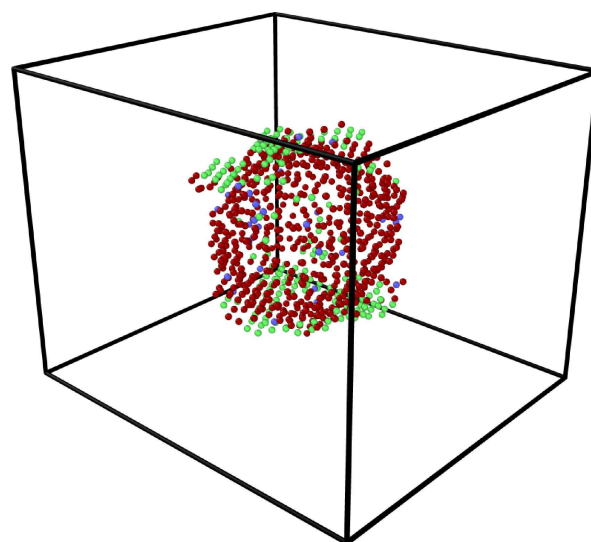
Figure 10. End state of 6% porosity LIME simulation; particles analyzed by bond-angle analysis and classified as hcp (removed from display for visual clarity), fcc (green), bcc (blue), or other (red). In this image, the original void remained intact.
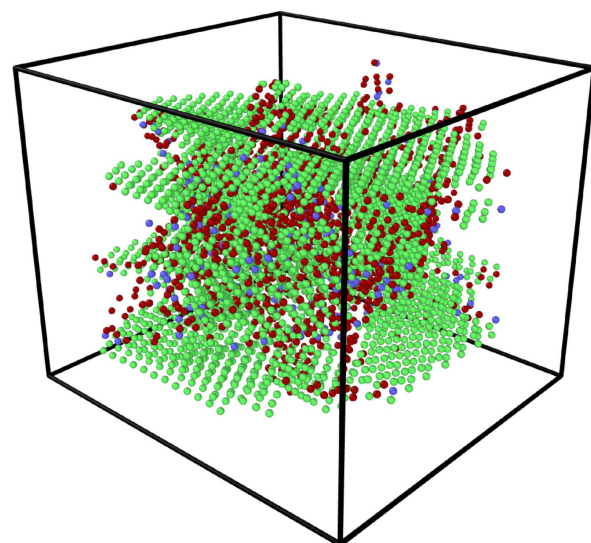
Figure 11. End state of 10% porosity LIME simulation; particles analyzed by bond-angle analysis and classified as hcp (removed from display for visual clarity), fcc (green), bcc (blue), or other (red). In this image, the original void collapsed and periodic-boundary-spanning disorder resulted.

geneous simulation cell. To elucidate the local structure, lattice analysis was performed using the bond-angle analysis function in Ovito [92]. In these figures, results are provided for ambient reference state RVEs seeded with a 6% porosity and 10% porosity, respectively. The initial crystal lattice is hcp; in these images, the hcp particles have been deleted and the remaining fcc (green), bcc (blue) and other (red) particles are shown. The fcc particles are commonly ob-

served at planar interfaces between hcp particles and a non-crystalline local region, or where slip defects have occurred. In the 6 % porosity case, the void remains intact, while in the 10 % porosity case, the void has collapsed and the resulting disorder traverses the RVE periodic boundaries in two dimensions (and very nearly all three). These non-reactive, hydrostatic, equilibrium simulations of pores do not result in the jetting or high-temperature reactive response observed in the shock simulations.

2.3 Speculative HMS for Non-Reactive Taylor Impact

A HMS macroscale model invoking LIME or other similar, computationally expensive RVEs would quickly become intractable if the microscale model must be evaluated for each element at every time step. Thus, we have sought ways to accelerate microscale modeling and overall macroscale time-to-solution. In general, multiscale modelling is a divide-and-conquer endeavor. Sub-models are chosen to resolve phenomenon at individual spatial and temporal scales, and then these sub-models are combined together to form a multiscale model. Towards this end, a multiscale model of the dynamic deformation of RDX is under development using a HMS scale-bridging computational framework [72,93]. In the following subsections, we will describe the HMS approach to develop a multiscale model of RDX, the use of adaptive sampling techniques in HMS to reduce computational cost of the model, and the development of new algorithms in HMS for speculative evaluation of sub-models to further reduce computational cost.

2.3.1 HMS Framework

The HMS framework allows model developers to combine sub-models operating at individual spatial and temporal scales to form a multiscale model [93,94]. Each sub-model may be a complex parallel simulation code. Task-based evaluation of the sub-model components across disparate computational resources is orchestrated by the HMS framework during multiscale model evaluation. Mechanisms are provided in HMS to dynamically evaluate a sub-model from another model, to extract relevant data from completed sub-model evaluations, and to handle common errors encountered during sub-model evaluation. The HMS approach to multiscale model development is an example of the concept of Distributed Multiscale Computing (DMC), where multiscale simulations involve the orchestrated execution of individual sub-model components [48,51,95]. DMC has the potential to take full advantage of emerging exascale high performance computers, but challenges remain to manage these highly-dynamic computations on computers that have traditionally been used for monolithic codes employing domain decomposition. For example, the adaptive evaluation of surrogate models within DMC applications often

leads to an underutilization of computational resources that requires new algorithms to resolve, such as the speculative evaluation approaches developed in this article.

2.3.2 Multiscale Model Description

The multiscale model of RDX under consideration here consists of two sub-models: a continuum finite element macroscale model implemented in ALE3D [96], and a microscale model of RDX simulated using with the LAMMPS USER-DPD package. The macroscale model obtains the EOS of RDX directly through evaluation of a DPD-LAMMPS simulation. Specifically, the microscale DPD-LAMMPS simulation computes the temperature and pressure of RDX given a particular internal energy and mass density. Within the two-scale model, evaluation of the EOS with DPD-LAMMPS is automated by LIME [73]. For the simulations considered here, the DPD simulation cell is taken to be defect-free, non-reactive, $28 \times 14 \times 14$ hexagonal close-packed unit cells of RDX, for a total of 21,952 particles. A modified predictor-corrector integration scheme is used in the macroscale model to update energy as described in Wang *et al.* [97].

2.3.3 Adaptive Sampling

In order to reduce the cost of expensive multiscale models, adaptive sampling techniques have been developed within the HMS framework, and applied to multiscale modelling of RDX. For details we refer the reader to Leiter *et al.* [72] and Knap *et al.*, [93] but will briefly describe the method here. Adaptive sampling is an active learning method that constructs a set of local Gaussian process regression (GPR) surrogate models on-the-fly to replace the repeated evaluation of computationally expensive sub-models. In the case of the two-scale model of RDX, the GPR surrogate models serve to approximate the EOS computed from LIME. An error estimate of the GPR prediction is compared to a user-specified error tolerance parameter, $\tilde{e}_{tol}$, to determine if the GPR prediction is accurate enough to be used for a particular mass density and internal energy density, or whether the LIME model must be evaluated instead. In the case where LIME is called, the computed EOS is used to update the surrogate model. In principle, any surrogate modelling method that includes an error estimate, and which can be updated cheaply with new data, can be used for adaptive sampling. To keep surrogate model updates relatively cheap, rather than constructing a single GPR model over all the data, we build a number of local GPR models on a partition of the data. A parameter, d_{max}, restricts the total number of data contained in any local GPR model, and the collection of models is stored in a metric-tree database for quick access for interpolation and update.

Adaptive sampling has been shown to reduce computational cost for a variety of multiscale models, but in practice

suffers from the fact that the overall simulation is often highly load-imbalanced due to the unpredictable evaluation patterns of expensive sub-models and inexpensive surrogate models [72]. Often, the multiscale model executes on a high performance computer with a shared batch queue, where computational resources must be requested ahead of time for exclusive use over a period of time. It is difficult to select *a priori* an appropriate number of computational resources for simulations that use adaptive sampling, especially since it is common that fewer resources are utilized later in the simulation as the surrogate model is improved and fewer evaluations of the underlying sub-model are required. Some batch queues, such as Slurm with the *scontrol* command, allow running simulations to dynamically alter their allocated size, which could alleviate the load imbalance to some extent [98]. For example, when many sub-model evaluations are required, the simulation could acquire additional computational resources, or in the regime where the cheap surrogate model is evaluated more often, the simulation could release computational resources. However, not all batch queue systems allow for the dynamic resizing of running jobs and even Slurm's *scontrol* functionality does not work on all HPC architectures.

One strategy to avoid load imbalance issues entirely is to precompute the surrogate model ahead of time if evaluation of the sub-model is restricted to some portion of its configurational space, an idea explored in Wang *et al.* [97]. However, the evaluation region may not be known ahead of time, as it may depend on complex interactions between the many sub-models that form the multiscale model. Here, we propose an alternative strategy that uses unoccupied processors during multiscale model evaluation to perform speculative evaluations of sub-models. The results of these speculative sub-model evaluations are not used directly by other sub-models in the multiscale model hierarchy, but rather their purpose is to improve the accuracy of the surrogate model. If the speculative evaluations are able to reduce the number of sub-model evaluations required at later times in the multiscale model evaluation, they can help to reduce the overall computational cost. Our approach is somewhat similar in spirit, but not design, to the spatial adaptive sampling method introduced by Rouet-Leduc *et al.* [81]. In their method, rather than evaluate the sub-model directly at points supplied by a macroscale model, evaluations are collected at each time step, and new sampling points are chosen using a predictive scheme to reduce surrogate model error below a threshold. Then, the sub-model is evaluated in parallel at all sampling points and the surrogate model constructed and evaluated to inform the macroscale model. Our approach is different, as the sub-model is evaluated at points supplied by the macroscale model, and these evaluations are supplemented with bespoke speculative evaluations that serve to both improve the surrogate model at the current time step and also for future time steps of the multiscale model.

2.3.4 Speculative Evaluations for Adaptive Surrogate Modeling

There exist many possible algorithms to generate new speculative sub-model evaluations to improve the surrogate model. Speculative algorithms may utilize the surrogate model directly to select new sampling points to reduce uncertainty, for example as is the case in the work of Zhao *et al.* for active learning of GPR surrogates for fluid flow [99]. Other approaches may not examine the surrogate model at all, but instead may select, based on physical knowledge of the system being modelled, sampling points expected to be useful at later times in the simulation. For example, if modelling compression of a material, it may be useful to select speculative evaluation points with higher densities. Therefore, to support many possible speculative modelling approaches, we implement the speculative generation of new sub-model evaluations generically in the HMS framework. Two functions are required to implement a new speculative generation algorithm: 1) a function to generate a number of new sampling points for speculative sub-model evaluations; 2) a function to update the speculative algorithm with data from completed sub-model evaluations so that the speculative algorithm can adjust itself based upon data from previous sub-model evaluations.

Initially, two algorithms are implemented for the speculative generation of new evaluation points in the HMS framework. The first algorithm is Monte Carlo sampling. Given bounds $B_i = [l_i, u_i]$, $i = 1, \ldots, d$ where d is the number of inputs to the sub-model, the Monte Carlo algorithm generates speculative evaluation samples uniformly in B_i for all inputs. The sampling bounds are selected ahead of time, and therefore this method utilizes no information from the history of the running multiscale simulation. The second speculative generation algorithm is based on the construction of kernel density estimators [100,101] (KDE) and does take advantage of information from the running simulation in an attempt to predict more useful sampling points. Its algorithm is an inspired heuristic that models the distribution of data for the current and previous time step of the macroscale model as KDEs, and then numerically estimates another KDE, referred to as the forward KDE, for the density gradient at the next time step (not the density itself). In this context, the density we refer to is the 2-d probability distribution density. This forward KDE is sampled, and results where the forward KDE density is greater than current/prior density KDEs are returned for HMS sampling.

More specifically, the input points for creating a KDE fit for a given time step are the collection of (mass density, energy) pairs needed as inputs for EOS calculations. A Gaussian kernel with bandwidth of 0.04 and relative tolerance of 10^{-4} are used to fit a KDE for the collection. Given two KDEs, we may determine the probability density of the difference of original two KDEs. As our KDE implementation does not support the subtraction operator for KDE objects, we determine this "difference" KDE through numerical sam-

pling of the original KDEs and annihilation of nearby points, then fitting a new KDE to the remaining points. The source code for performing that operation, determining its convergence with numerical integration, and other aspects of the KDE speculative sampling is available upon reasonable request. Empirically, the use of consecutive difference KDEs allows the identification of probability densities that are useful for the generation of points for adaptive sampling in HMS, as shown in Table 2. The scheme does not assume any underlying physics or explicit knowledge of gradients. Instead, it uses a series of numerical operations and 6 KDEs. The first two (*A* and *B*), are simple KDE fits to the prior and current datasets, respectively. KDE *C* is the "difference" KDE described above, with *A* and *B* as original KDEs. KDE *D* is fit to results of sampling KDE *C*, after filtering samples to remove them in regions, where the probability density of *C* is lower than *A* or *B*. This procedure is repeated once more, with KDE *E* being fit to the numerical difference of KDEs *B* and *D*, and KDE *F* being fit to the results of sampling *E* and removing results, where the density of *E* is lower than that of *A*, *B*, or *D*. At the end of this procedure, the new KDE *F* should represent areas of phase space where density is growing and is undersampled. KDE *F* itself may be sampled, and samples where the density of *F* is greater than the density of *A*, *B* or *D* are used as candidate points for future HMS evaluations.

Figure 12 provides an example that demonstrates the result of this procedure, plotted in energy density, mass density space. Figure 12 (top) displays EOS evaluations within a simulation for a previous time step (blue) and current time step (red) and the corresponding difference distribution KDE *C* (grey). Figure 12 (bottom) displays the distribution of possible future states, KDE *F*, which is the ultimate result of the KDE scheme operating on the data in Figure 12 (top). Thus, Figure 12 (bottom) displays a distribution that may be more useful to sample for future HMS time steps than unbiased Monte Carlo sampling.

After speculative evaluations are generated, the error estimate of the surrogate model is computed at each speculative evaluation point. If the error estimate is less than $\tilde{e}_{tol}$, the speculative evaluation is discarded as it indicates that the surrogate model already has sufficient accuracy at the speculative evaluation point. If the error estimate is greater than $\tilde{e}_{tol}$, the speculative evaluation is scheduled to
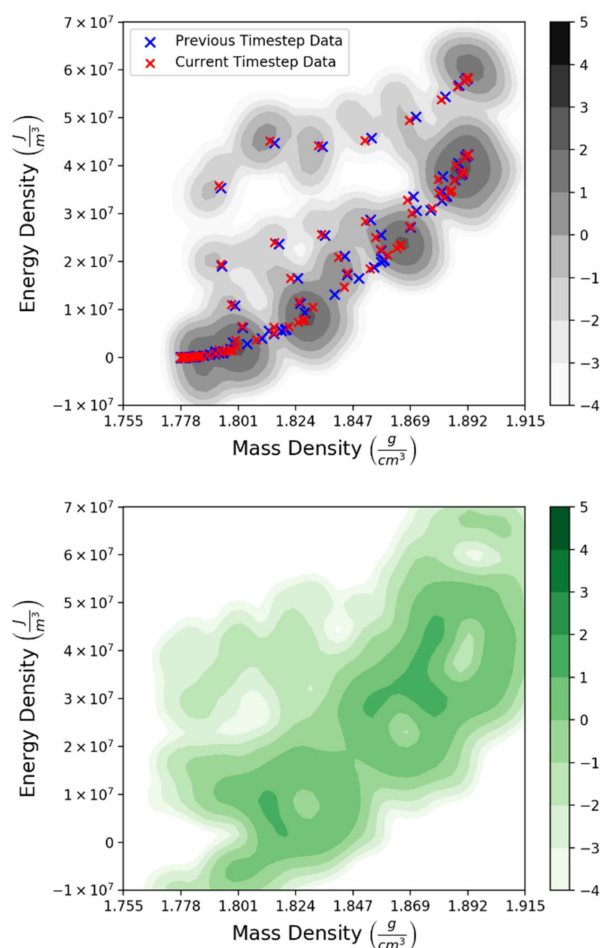
Figure 12. Example of KDE scheme operating on EOS evaluations from a previous (blue) and current (red) time step to produce the difference distribution KDE *C* (grey, upper frame). The scheme produces a distribution of possible future states, KDE *F* (green, bottom frame).

be executed on unoccupied processors during evaluation of the multiscale model. For details of scheduling of sub-model evaluations on computational resources in the HMS framework, see Knap *et al.* [93]. Speculative evaluations are given the lowest scheduling priority so that they are never executed before regular evaluations. Regular evaluations are those that originate directly from other sub-models, for example, the EOS evaluations requested by ALE3D in the multiscale model of RDX. In fact, to ensure that speculative evaluations do not interfere at all with evaluation of the multiscale model, we go a step further and modify the scheduling algorithm in HMS to mark speculative evaluations pre-emptable, meaning that their evaluation may be immediately stopped and replaced with a regular evaluation if any regular evaluations are present in the scheduling queue. If the speculative evaluation is pre-empted by a regular evaluation, its state is discarded and it is placed back into the scheduling queue.

Table 2. Wall-clock time for Taylor Impact simulations with 3240 processor cores.

Speculative Algorithm	Mean Wall-Clock Time (h)	Minimum Wall-Clock Time (h)	Mean Number Failed EOS Interpolations
No Speculative Evaluations	15.6	13.9	2831
Monte Carlo	14.4	13.5	1847
KDE	11.1	8.0	1385

2.3.5 Taylor Impact Simulation Setup

We evaluate performance of the speculative evaluation algorithms for the multiscale simulation of a Taylor impact experiment, an experiment commonly used to characterize dynamic deformation of materials. The simulation setups are identical to those presented in Leiter *et al.* [72]. In a Taylor impact experiment, a cylinder of material, in this case RDX, travels at a constant initial velocity and impacts a rigid anvil. The cylinder we model has initial velocity of 200 m/s, height of 1.27 cm, and radius of 0.476 cm. The ALE3D macroscale model is evaluated under axisymmetric conditions so that the RDX cylinder is decomposed into 1600 first-order quadrilateral elements. An adaptive time step with initial time step size of 0.001 μs and maximum allowable time step of 0.012 μs is used, and a total of 20 μs of the model is simulated for a total of 1676 time steps. Simulations are executed on the "Thunder" high performance computer at the Air Force Research Laboratory, containing a 36 core 2.3 GHz Intel Xeon Haswell processor on each compute node. For evaluation of the multiscale model, one processor core is assigned to the ALE3D macroscale model, six processor cores for the HMS framework (five cores for surrogate model evaluation, update, and generation of speculative evaluations, and one core to manage scheduling and execution of the microscale sub-model), and the remaining processor cores are dedicated to sub-model evaluation.

2.3.6 Results

We compare performance of the two speculative evaluation algorithms, Monte Carlo and KDE, to the case where no speculative evaluations are performed for the simulation of the Taylor impact experiment. A total of 3240 processor cores are allocated to each simulation. For the Monte Carlo generation of speculative evaluations, the bounds are set to $B_1 = ([1.7 \frac{g}{cm^3}, 2.1 \frac{g}{cm^3}])$ for mass density, and $B_2 = [0 \frac{J}{m^3}, 2 \times 10^8 \frac{J}{m^3}]$ for internal energy density. For adaptive sampling, $\tilde{e}_{tol}$ is set to 0.005, d_{max} to 50, and the GPR kernel is chosen to be squared exponential. These settings were shown in previous work to produce solutions with reasonable accuracy. Calls to LIME for computing the EOS are executed on 64 processor cores.

The total wall-clock time required to complete the simulation for the three cases of no speculative evaluations, Monte Carlo speculative evaluations, and KDE speculative evaluations are presented in Table 2. Since there is inherent randomness in the simulations, both due to the asynchronous nature of the computations and in the speculative algorithms themselves, each case was executed five times, and the mean time and minimum time of these runs is given. The case without speculative evaluation has the longest wall-clock time and the case with the KDE sampling has the shortest, both in mean and minimum.

For the runs with the minimum wall-clock time for each speculative algorithm, we plot the overall processor core utilization in Figure 13. The case with no speculative evaluations shows processor utilization fluctuating dramatically over the course of the simulation, and overall it exhibits poor processor utilization, especially towards the end of the simulation. The overall processor utilization is only 26% for the simulation with no speculative evaluations. However, processor utilization is nearly 100% in the Monte Carlo case and 94% in the KDE case. The KDE speculative simulation shows a quick drop in processor utilization at the beginning of the simulation. This is due to the bootstrapping of the algorithm as it requires a few time steps of the multiscale model to finish before the KDE model can be constructed. In Figure 13, we also plot the number of evaluations of each type, regular and speculative evaluations, which are
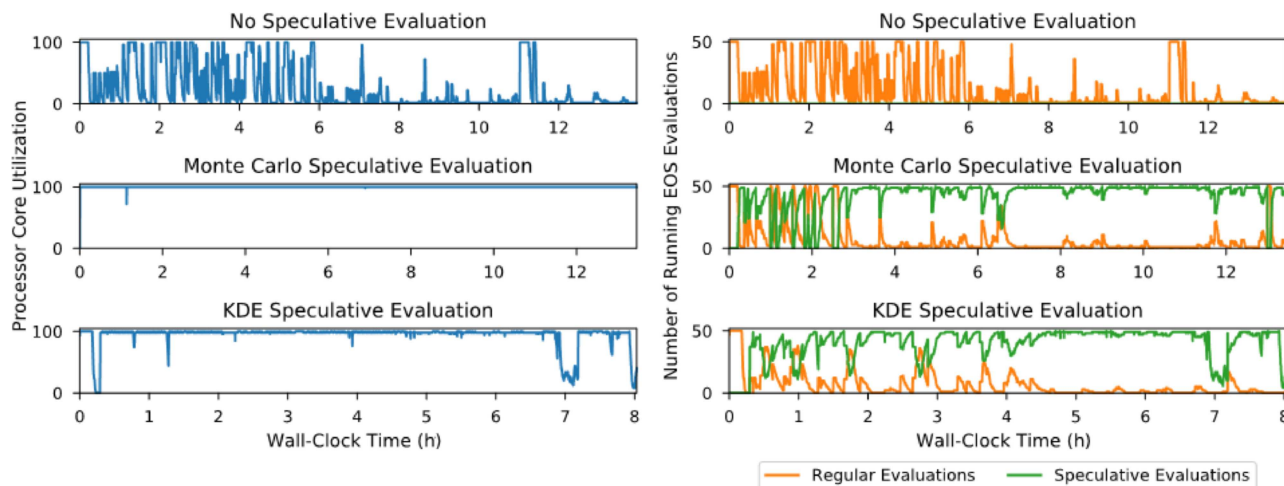
Figure 13. Processor utilization for simulations using each speculative evaluation algorithm. Number of running regular evaluations and speculative evaluations over time for each speculative evaluation algorithm.

running over the course of the simulation. For the simulations using speculative evaluations, it is clear that the speculative evaluations are executed when few regular evaluations are running. The simulations with speculative evaluations are able to saturate all available processor cores. However, just because these simulations are able to occupy processor cores with speculative computations does not necessarily mean that the speculative evaluations are useful. To be useful, the speculative evaluations must improve the accuracy of the surrogate model in regions of interest to the multiscale model so that fewer microscale EOS evaluations are required over the course of the simulation. To explore the degree to which speculative evaluations improve the accuracy of the surrogate model, in Table 2 we provide the mean number of failed EOS interpolations of the surrogate model. Failed EOS interpolations are those that necessitate an evaluation of the microscale model in adaptive sampling, and are due to a lack of accuracy and high uncertainty in the surrogate model. The number of failed interpolations is fewer for the simulations with speculative evaluations, with the KDE speculative evaluation scheme having the fewest. Therefore, the speculative evaluations do appear to help improve the surrogate model so that fewer microscale EOS evaluations are required over the course of the simulation.

To assess the improvement of the speculative evaluation algorithms on the scalability of the model, we also run the Taylor impact simulation with 6480 and 12960 total processor cores. As in the 3240 processor core simulations, we run each case five times to account for the randomness in the simulations. The mean wall-clock time required to complete these simulations is plotted in Figure 14, along with the cases that use 3240 processor cores. The simulations with no speculative evaluations and with Monte Carlo speculative evaluations both exhibit poor scalability. The use of Monte Carlo speculative evaluations improves the performance marginally over the case without any spec-

ulative evaluations. The simulations that use the KDE speculative evaluations exhibit better scalability and the best performance overall.

Clearly, the use of speculative evaluations on unoccupied computational resources does offer some benefit to improve the overall performance of the multiscale model. For the Taylor impact simulation considered here, the KDE speculative generation algorithm offers better performance than the Monte Carlo scheme, likely due to the fact that the KDE scheme attempts to predict useful evaluation points based upon the history of the model. In contrast, the Monte Carlo approach uses no information from the running simulation other than whether a randomly selected trial point can already be successfully evaluated by the GPR surrogate model, and its performance is relatively poor.

3 Discussion

3.1 DPD-RX Shock

Defect-free and porous samples of RDX have been simulated under shock conditions to demonstrate the influence of microstructural features on material performance using explicit large-scale computational capabilities. In the absence of defects, the reaction wave and shock wave are observed to converge and transition to a steady-state reaction wave on nanosecond time-scales under strong shock conditions. By introducing porosity into the samples, the transition to a steady-state reaction wave is observed to occur at weaker shock strengths as compared to the defect-free sample. In response to shock, the pores within the RDX sample collapse, creating localized hot-spots that lead to the initiation of chemistry and subsequent growth of reaction volumes as RDX decomposes into intermediate and product gas species. With sufficient energy deposited at the defect site during shock, the reaction volume grows and coalesces with neighboring reaction volumes, eventually forming a steady-state reaction wave that propagates through the material.

A number of factors dictate whether a reaction wave will form, including the porosity of the sample, the pore size distribution and the shock strength. This work did not consider pores that may be present at grain intersections, or effects of grain boundaries as discussed in the introduction. The CG/DPD modeling framework is well-suited for modeling nm-sized pores under strong shock or fast cook-off conditions, enabling simulations at vastly different length and time scales as compared to atomic-scale simulations. However, current CG simulation capabilities are unable to simulate the full range of pore sizes that are observed in experimental pore size distributions. Methods that couple these CG methods with continuum length and times scales, such as the HMS approach presented in this work, are promising paths to further explore the role of microstructure on EM performance.
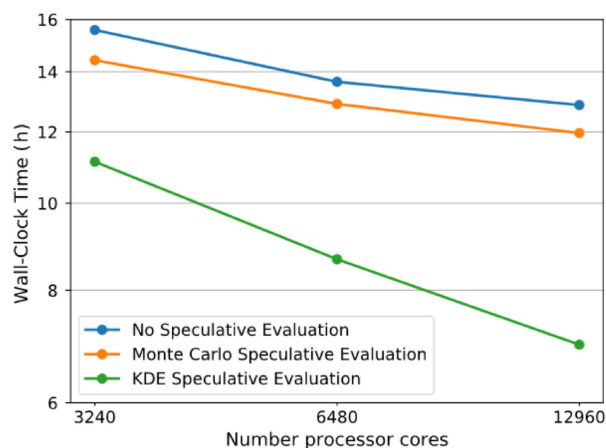
Figure 14. Log-log plot of mean wall-clock time for Taylor Impact simulations that use different speculative evaluation algorithms.

While the DPD-RX framework reduces the time-to-solution for simulating micron-sized samples over ns-timescales from *O*(*years*) using the only viable atomistic-scale approach to *O*(*hours*) on modern supercomputers [87], it does require investment into the development of CG models and methods capable of capturing the condensed-phase and gas-phase physics. One such aspect that requires further investigation and development is the PGM model. The particle interaction model for the PGM presented in this work was parameterized for a limited range of chemical states typically present under the extreme conditions of shock and thermal loading. PGM model improvements will require significant effort to further sample the reacting environment in a statistically-reliable manner, which is dependent upon both the density and species concentrations. However, recent development of a many-body, CG model (CG-MB) that accurately describes the thermodynamic behavior of molecular mixtures is a promising alternative to this tedious approach [102]. Moreover, CG-MB models may be a viable path for extending the length scales that can be simulated using CG models by going beyond the typical hard-core particle forcefields, and replacing them with these CG-MB models [102–106]. A many-body force-field based upon a free-energy EOS has many attributes as a CG model, including robust transferability and scalability. CG-MB models are dependent upon both the local density and temperature. As such, while an isothermal simulation method is suitable, implementing a CG-MB model at constant-energy conditions requires an appropriate method. Within the DPD framework, two methods have been re-formulated for simulating a CG-MB at constant energy [107, 108]. While these methods have similarities, the latter method has been formulated in a bottom-up fashion, such that the thermodynamic behavior of the higher resolution model used to build a CG model is recovered, whereas the former method recovers the Navier-Stokes behavior in the opposing limiting regime. Presently, only the work of Faure and Maillet has been extended to implicitly simulate chemical reactivity [109].

3.2 Porous LIME

In sections 2.1 and 3.1, CG RDX shock for systems at 2% and 4% porosity resulted in pore collapse and ultimately reactions, indicating a significant increase in particle internal temperatures. For the non-reactive hydrostatic LIME RVE presented in section 2.2, addition of 2–4% porosity only resulted in a moderate increase of pressure and temperature, roughly ~0.3 GPa and 20 K, respectively. At low porosities, no pore collapse was observed. This was the case for a reference system at either ambient or high-density conditions. Although the DPD-RX simulations and LIME RVE results cover a slightly different range of states, the difference between results from those two methods indicates that the pore response demonstrated in section 2.1 is largely driven

by the loading condition of uniaxial shock compression (wave propagation), as opposed to the nominally homogeneous deformation in the LIME RVE.

The addition of microstructure to a multiscale RVE, even in a non-reactive model, is a task that may spiral into considerable complexity. When used as part of a HMS simulation, the macroscale (in our case, a finite element simulation) should carry additional per-element history variables to describe the microstructure (in our case, porosity) as needed to both instantiate the RVE and propagate the microstructure forward in time. The macroscale may have other material models that affect the microstructure history variables, such as pore collapse being linked to a macroscale plasticity model. More complex RVEs may be designed to differentiate between void space implemented as pores in solids, versus void space that is gas-filled space between irregular solid grains that cannot perfectly fill space. Distributions of void shapes and sizes may be addressed through more complicated instantiations of larger RVEs. If pores previously collapsed in the RVE for a finite element, it may also be appropriate to re-instantiate the RVE for that element at future time steps not as a solid crystal, but rather as a partially disordered system. There are also fundamental issues that we have not addressed in this work, such as simulating a directional shock wave propagating through microstructure when wanting to extract hydrostatic information from the RVE. We speculate that in future detailed HMS simulations there may not be "one RVE to rule them all", but rather an ensemble of RVEs that will be used to extract different macroscale responses, and be spawned in parallel to sample stochastic response. Future work must also expand the microstructure-aware RVE to a reactive model, and be able to describe in detail the end state of the RVE microstructure for its propagation at the macroscale.

3.3 Speculative HMS

The HMS approach to multiscale model development is quite practical as it allows modelers to combine existing codes together, *e.g.*, ALE3D and LAMMPS, to model a multiscale phenomenon of interest. By utilizing existing codes to construct a multiscale model, HMS takes advantage of the significant investment made on their development. The resulting multiscale model involves adaptive execution and data exchange between the individual sub-model components. Such computation by its nature is adaptive and asynchronous. When adaptive sampling techniques to construct surrogate models are introduced into a multiscale model, the resulting computation is even more dynamic, and presents a challenge for the efficient utilization of computational resources on high-performance computers. In this article, we introduced a speculative evaluation method in the HMS computational framework to take advantage of idle processors during multiscale model evaluation. The idle

processors are used to evaluate sub-models to improve the accuracy and expand the domain of applicability of the surrogate model built during adaptive sampling. To assess the effectiveness of the speculative evaluation method, we demonstrate its use for a multiscale model of RDX deformation. The speculative evaluation method is shown to perform useful computation on processor cores that would otherwise be unused and reduces the overall wall-clock time to evaluate the multiscale model.

A key consideration for the speculative evaluation method is the choice of algorithm to generate sampling points for sub-model evaluation. The sampling points must serve to improve the surrogate model in regions of interest to the multiscale model, otherwise the speculative evaluations have no utility. We implement two methods for speculative point generation, a Monte Carlo approach that generates sampling points uniformly in a specified region, and a KDE based approach that attempts to use the recent history of sub-model evaluations to select sampling points. Our results show the KDE based approach performs better than Monte Carlo in the multiscale model of RDX deformation. There is certainly much room for improvement in these algorithms. In contrast to the Monte Carlo scheme, which uses no information from the running multiscale model evaluation (apart from discarding the speculative evaluations that can be accurately computed by the GPR surrogate), the KDE based approach does adjust its sampling region as the multiscale model is evaluated. Importantly, neither method uses the surrogate model directly for the selection of sampling points. The GPR surrogate model encodes information about its uncertainty and speculative sampling points could be chosen to reduce this uncertainty the most. We believe that a blended approach will probably be best: a method that uses information from the running multiscale model to identify new sampling regions to explore along with information from the surrogate model to select points within the identified region that reduce uncertainty the most. It should also be pointed out that the surrogate model constructed for the EOS of RDX in this application has low-dimensionality. For higher-dimensional problems, such as when microstructure is incorporated into the model, both the construction of the surrogate model itself, as well as the generation of speculative sampling points, will become a challenge.

Although speculative evaluations do improve the performance of the multiscale model of RDX, it is by no means a panacea to the issues of adaptive computation on high-performance computers. For example, although CPU utilization increases from 26 % to 94 % for no speculative evaluations versus KDE speculative evaluations on 3240 processors, an improvement of a factor of 3.6, the overall speedup is only 1.7. If mechanisms were available to facilitate the fine-grained use of computational resources, then it is likely that using no speculative evaluations would require fewer computational resources than using speculative evaluations. In other words, the utility of speculative evalua-

tions is for the common situation of running on a high-performance computer with a shared batch queue that assigns a fixed allocation of computational resources. Certainly, the use of speculative evaluations does take advantage of unused computational resources, and this can be seen most clearly in the improved scalability of the model. From 3240 to 12960 processors, the mean wall-clock time speedup is only 1.2 for the case without speculative evaluations, but is 1.6 for the case with KDE speculative evaluations. This is by no means perfect scalability, but it is an improvement and could possibly be further improved with the development of better algorithms for the selection of speculative evaluation points. Future work will need to evaluate such algorithms in a high-dimensional input space as the complexity of the microscale model increases (*e.g.* inclusion of porosity or reactivity variables in the surrogate model).

4 Conclusion

In this article, we have demonstrated new capabilities for investigation of microstructure in energetic material response for both explicit large-scale and multiscale simulations. The wall-clock time required for these future detailed multiscale simulations may be offset in part by advances in speculative simulation and aggressive creation of surrogate models described in this work, leveraging any available CPU cores on supercomputers. The capabilities here, while demonstrated for an impact simulation of a model of RDX, may be adapted to a variety of reactive systems, including metallic reactive materials. Future work will involve improvements in the microscale (CG) model, enhanced transfer of information between scales, and HMS advancements for scale-bridging in time. Our goal is a complete and accurate hierarchical multiscale simulation for reactive response of energetic materials, and we continue to make progress on the necessary components for HMS.

References

[1] Y. Duan, P. A. Kollman, Pathways to a Protein Folding Intermediate Observed in a 1-Microsecond Simulation in Aqueous Solution, *Science* **1998**, *282*, 740–744.
[2] D. E. Shaw, P. Maragakis, K. Lindorff-Larsen, S. Piana, R. O. Dror, M. P. Eastwood, J. A. Bank, J. M. Jumper, J. K. Salmon, Y.

Shan, W. Wriggers, Atomic-Level Characterization of the Structural Dynamics of Proteins, *Science* **2010**, *330*, 341–346.

[3] TOP500. https://www.top500.org/statistics/perfdevel/

[4] M. M. Sultan, R. A. Denny, R. Unwalla, F. Lovering, V. S. Pande, Millisecond dynamics of BTK reveal kinome-wide conformational plasticity within the apo kinase domain, *Sci. Rep.* **2017**, *7*, 15604.

[5] W. Du, P. G. Bolhuis, Equilibrium kinetic network of the villin headpiece in implicit solvent, *Biophys. J.* **2015**, *108*, 368–378.

[6] P. G. Bolhuis, D. Chandler, C. Dellago, P. L. Geissler, Transition path sampling: throwing ropes over rough mountain passes, in the dark, *Annu. Rev. Phys. Chem.* **2002**, *53*, 291–318.

[7] B. C. Barnes, B. C. Knott, G. T. Beckham, D. T. Wu, A. K. Sum, Reaction coordinate of incipient methane clathrate hydrate nucleation, *J. Phys. Chem. B* **2014**, *118*, 13236–13243.

[8] T. C. Germann, K. Kadau, Trillion-Atom Molecular Dynamics Becomes a Reality, *Int. J. Mod. Phys. C* **2008**, *19*, 1315–1319.

[9] T. P. Senftle, S. Hong, M. M. Islam, S. B. Kylasa, Y. Zheng, Y. K. Shin, C. Junkermeier, R. Engel-Herbert, M. J. Janik, H. M. Aktulga, T. Verstraelen, A. Grama, A. C. T. van Duin, The ReaxFF reactive force-field: development, applications and future directions, *npj Comput. Mater.* **2016**, *2*, 15011.

[10] M. A. Wood, M. J. Cherukara, E. Antillon, A. Strachan, Molecular Dynamics Simulations of Shock Loading of Materials: A Review and Tutorial, *Rev. Comput. Chem.*, **2017**.

[11] A. C. van Duin, S. Dasgupta, F. Lorant, W. A. Goddard, ReaxFF: A Reactive Force Field for Hydrocarbons, *J. Phys. Chem. A* **2001**, *105*, 9396–9409.

[12] K. Chenoweth, A. C. van Duin, W. A. Goddard III, ReaxFF Reactive Force Field for Molecular Dynamics Simulations of Hydrocarbon Oxidation, *J. Phys. Chem. A* **2008**, *112*, 1040–1053.

[13] T.-R. Shan, R. R. Wixom, A. P. Thompson, Extended asymmetric hot region formation due to shockwave interactions following void collapse in shocked high explosive, *Phys. Rev. B* **2016**, *94*, 054308.

[14] J. K. Brennan, M. Lísal, J. D. Moore, S. Izvekov, I. V. Schweigert, J. P. Larentzos, Coarse-Grain Model Simulations of Nonequilibrium Dynamics in Heterogeneous Materials, *J. Phys. Chem. Lett.* **2014**, *5*, 2144–2149.

[15] J. B. Maillet, L. Soulard, G. Stoltz, A reduced model for shock and detonation waves. II. The reactive case, *Europhys. Lett.* **2007**, *78*, 68001.

[16] M. Lísal, J. K. Brennan, W. R. Smith, Mesoscale simulation of polymer reaction equilibrium: combining dissipative particle dynamics with reaction ensemble Monte Carlo. I. Polydispersed polymer systems, *J. Chem. Phys.* **2006**, *125*, 164905.

[17] H. Fellermann, S. Rasmussen, H.-J. Ziock, R. V. Solé, Life Cycle of a Minimal Protocell-A Dissipative Particle Dynamics Study, *Artificial Life* **2007**, *13*, 319–345.

[18] H. Liu, H.-J. Qian, Y. Zhao, Z.-Y. Lu, Dissipative particle dynamics simulation study on the binary mixture phase separation coupled with polymerization, *J. Chem. Phys.* **2007**, *127*, 144903.

[19] M. Lísal, J. K. Brennan, W. R. Smith, Mesoscale simulation of polymer reaction equilibrium: Combining dissipative particle dynamics with reaction ensemble Monte Carlo. II. Supramolecular diblock copolymers, *J. Chem. Phys.* **2009**, *130*, 104902.

[20] A. V. Berezkin, Y. V. Kudryavtsev, Simulation of End-Coupling Reactions at a Polymer-Polymer Interface: The Mechanism of Interfacial Roughness Development, *Macromolecules* **2011**, *44*, 112–121.

[21] A. Strachan, B. L. Holian, Energy exchange between mesoparticles and their internal degrees of freedom, *Phys. Rev. Lett.* **2005**, *94*, 014301.

[22] K. Lynch, A. Thompson, A. Strachan, Coarse grain modeling of spall failure in molecular crystals: role of intra-molecular degrees of freedom, *Modell. Simul. Mater. Sci. Eng.* **2009**, *17*, 015007.

[23] E. Antillon, K. Banlusan, A. Strachan, Coarse grain model for coupled thermo-mechano-chemical processes and its application to pressure-induced endothermic chemical reactions, *Modell. Simul. Mater. Sci. Eng.* **2014**, *22*, 025027.

[24] E. Antillon, A. Strachan, Mesoscale simulations of shockwave energy dissipation via chemical reactions, *J. Chem. Phys.* **2015**, *142*, 084108.

[25] M. M. Islam, M. Cherukara, E. Antillon, A. Strachan. Shock-Induced Chemistry: Molecular Dynamics and Coarse Grain Modeling. in: *Computational Approaches for Chemistry Under Extreme Conditions* (N. Goldman, ed., Springer International Publishing, Cham **2019**, 187–208.

[26] H. S. Fogler, *Elements of Chemical Reaction Engineering.* Prentice Hall. Englewood Cliffs, NJ, 1992.

[27] J. B. Maillet, E. Bourasseau, N. Desbiens, G. Vallverdu, G. Stoltz, Mesoscopic simulations of shock-to-detonation transition in reactive liquid high explosive, *Europhys. Lett.* **2011**, *96*, 68007.

[28] M. P. Kroonblawd, T. D. Sewell, J. B. Maillet, Characteristics of energy exchange between inter- and intramolecular degrees of freedom in crystalline 1,3,5-triamino-2,4,6-trinitrobenzene (TATB) with implications for coarse-grained simulations of shock waves in polyatomic molecular crystals, *J. Chem. Phys.* **2016**, *144*, 064501.

[29] B. C. Barnes, J. K. Brennan, E. F. C. Byrd, S. Izvekov, J. P. Larentzos, B. M. Rice. Toward a Predictive Hierarchical Multiscale Modeling Approach for Energetic Materials. in: *Computational Approaches for Chemistry Under Extreme Conditions* (N. Goldman, ed., Springer International Publishing, Cham **2019**, 229–282.

[30] N. Chennamsetty, H. Bock, M. Lísal, J. K. Brennan. An Introduction to Coarse-Graining Approaches: Linking Atomistic and Mesoscales. in: *Process Systems Engineering: Vol. 6 Molecular Systems Engineering* (C. Adjiman, A. Galindo, eds), WILEY-VCH Verlag GmbH & Co., KGaA, Weinheim, **2011**.

[31] F. Müller-Plathe, Coarse-Graining in Polymer Simulation: From the Atomistic to the Mesoscopic Scale and Back, *ChemPhysChem* **2002**, *3*, 754–769.

[32] V. Tozzini, Coarse-grained models for proteins, *Curr. Opin. Struct. Biol.* **2005**, *15*, 144–150.

[33] C. Peter, K. Kremer, Multiscale simulation of soft matter systems – from the atomistic to the coarse-grained level and back, *Soft Matter* **2009**, *5*, 4357–4366.

[34] W. G. Noid, Perspective: Coarse-grained models for biomolecular systems, *J. Chem. Phys.* **2013**, *139*, 090901.

[35] W. Schommers, A pair potential for liquid rubidium from the pair correlation function, *Phys. Lett. A* **1973**, *43*, 157.

[36] S. Izvekov, P. W. Chung, B. M. Rice, The multiscale coarse-graining method: assessing its accuracy and introducing density dependent coarse-grain potentials, *J. Chem. Phys.* **2010**, *133*, 064109.

[37] S. Izvekov, P. W. Chung, B. M. Rice, Particle-based multiscale coarse graining with density-dependent potentials: application to molecular crystals (hexahydro-1,3,5-trinitro-s-triazine), *J. Chem. Phys.* **2011**, *135*, 044112.

[38] S. Izvekov, G. A. Voth, A Multiscale Coarse-Graining Method for Biomolecular Systems, *J. Phys. Chem. B* **2005**, *109*, 2469–2473.

[39] S. Izvekov, G. A. Voth, Multiscale coarse graining of liquid-state systems, *J. Chem. Phys.* **2005**, *123*, 134105.

[40] L. Lu, S. Izvekov, A. Das, H. C. Andersen, G. A. Voth, Efficient, Regularized, and Scalable Algorithms for Multiscale Coarse-Graining, *J. Chem. Theory Comput.* **2010**, *6*, 954–965.

[41] W. G. Noid, J. W. Chu, G. S. Ayton, V. Krishna, S. Izvekov, G. A. Voth, A. Das, H. C. Andersen, The multiscale coarse-graining method. I. A rigorous bridge between atomistic and coarse-grained models, *J. Chem. Phys.* **2008**, *128*, 244114.

[42] W. G. Noid, P. Liu, Y. Wang, J. W. Chu, G. S. Ayton, S. Izvekov, H. C. Andersen, G. A. Voth, The multiscale coarse-graining method. II. Numerical implementation for coarse-grained molecular models, *J. Chem. Phys.* **2008**, *128*, 244115.

[43] M. S. Shell, The relative entropy is fundamental to multiscale and inverse thermodynamic problems, *J. Chem. Phys.* **2008**, *129*, 144108.

[44] J. D. Moore, B. C. Barnes, S. Izvekov, M. Lísal, M. S. Sellers, D. E. Taylor, J. K. Brennan, A coarse-grain force field for RDX: Density dependent and energy conserving, *J. Chem. Phys.* **2016**, *144*, 104501.

[45] B. M. Rice, T. D. Sewell. Equilibrium Molecular Dynamics Simulations. in: *Static Compression of Energetic Materials* (S. M. Peiris, G. J. Piermarini, eds), Springer-Verlag, Berlin Heidelberg, **2008**.

[46] D. E. Taylor, B. M. Rice. Quantum-informed multiscale M&S for energetic materials. in: *Advances in Quantum Chemistry: Energetic Materials* (J. R. Sabin, ed. Vol 69. Academic Press, Cambridge, MA **2014**, 171–204.

[47] R. A. Pesce-Rodriguez, S. M. Piraino, *Characterization of Cyclohexanone Inclusions in Class 1 RDX*, ARL-TR-6962, U.S. Army Research Laboratory, **2014**.

[48] A. G. Hoekstra, B. Chopard, D. Coster, S. Portegies Zwart, P. V. Coveney, Multiscale computing for science and engineering in the era of exascale performance, *Philos. Trans. R. Soc. London Ser. A* **2019**, *377*, 20180144.

[49] D. Stephenson, J. R. Kermode, D. A. Lockerby, Accelerating multiscale modelling of fluids with on-the-fly Gaussian process regression, *Microfluid. Nanofluid.* **2018**, *22*, 139.

[50] W. A. Curtin, R. E. Miller, A perspective on atomistic-continuum multiscale modeling, *Modell. Simul. Mater. Sci. Eng.* **2017**, *25*, 071004.

[51] S. Alowayyed, D. Groen, P. V. Coveney, A. G. Hoekstra, Multiscale computing in the exascale era, *J. Comput. Sci.* **2017**, *22*, 15–25.

[52] S. Schmauder, I. Schäfer, Multiscale materials modeling, *Mater. Today* **2016**, *19*, 130–131.

[53] M. G. D. Geers, J. Yvonnet, Multiscale modeling of microstructure-property relations, *MRS Bull.* **2016**, *41*, 610–616.

[54] J. A. Elliott, Novel approaches to multiscale modelling in materials science, *Int. Mater. Rev.* **2013**, *56*, 207–225.

[55] M. A. Wood, D. E. Kittell, C. D. Yarrington, A. P. Thompson, Multiscale modeling of shock wave localization in porous energetic material, *Phys. Rev. B* **2018**, *97*, 014109.

[56] S. Jiang, J. Tao, T. D. Sewell, Z. Chen, Hierarchical multiscale simulations of crystalline β-octahydro-1,3,5,7-tetranitro-1,3,5,7-tetrazocine (β-HMX): Generalized interpolation material point method simulations of brittle fracture using an elastodamage model derived from molecular dynamics, *Int. J. Damage Mech.* **2017**, *26*, 293–313.

[57] M. J. Cawkwell, D. S. Montgomery, K. J. Ramos, C. A. Bolme, Free Energy Based Equation of State for Pentaerythritol Tetranitrate, *J. Phys. Chem. A* **2017**, *121*, 238–243.

[58] M. J. Cawkwell, D. J. Luscher, F. L. Addessio, K. J. Ramos, Equations of state for the α and γ polymorphs of cyclotrimethylene trinitramine, *J. Appl. Phys.* **2016**, *119*, 185106.

[59] K. Lee, K. Joshi, S. Chaudhuri, D. S. Stewart, Mirrored continuum and molecular scale simulations of the ignition of high-pressure phases of RDX, *J. Chem. Phys.* **2016**, *144*, 184111.

[60] P. Lafourcade, C. Denoual, J.-B. Maillet, Mesoscopic constitutive law with nonlinear elasticity and phase transformation for the twinning-buckling of TATB under dynamic loading, *Phys. Rev.* **2019**, *3*, 053610.

[61] H. K. Springer, S. Bastea, A. L. Nichols, C. M. Tarver, J. E. Reaugh, Modeling The Effects of Shock Pressure and Pore Morphology on Hot Spot Mechanisms in HMX, *Propellants Explos. Pyrotech.* **2018**, *43*, 805–817.

[62] R. A. Austin, N. R. Barton, J. E. Reaugh, L. E. Fried, Direct numerical simulation of shear localization and decomposition reactions in shock-loaded HMX crystal, *J. Appl. Phys.* **2015**, *117*, 185902.

[63] S. Kim, C. Miller, Y. Horie, C. Molek, E. Welle, M. Zhou, Computational prediction of probabilistic ignition threshold of pressed granular octahydro-1,3,5,7-tetranitro-1,2,3,5-tetrazocine (HMX) under shock loading, *J. Appl. Phys.* **2016**, *120*, 115902.

[64] E. J. Welle, C. D. Molek, R. R. Wixom, P. Samuels, Microstructural effects on the ignition behavior of HMX, *J. Phys. Conf. Ser.* **2014**, *500*, 052049.

[65] O. Sen, N. K. Rai, A. S. Diggs, D. B. Hardin, H. S. Udaykumar, Multi-scale shock-to-detonation simulation of pressed energetic material: A meso-informed ignition and growth model, *J. Appl. Phys.* **2018**, *124*, 085110.

[66] N. K. Rai, H. S. Udaykumar, Three-dimensional simulations of void collapse in energetic materials, *Phys. Rev. Fluids* **2018**, *3*, 033201.

[67] O. Sen, N. J. Gaul, K. K. Choi, G. Jacobs, H. S. Udaykumar, Evaluation of kriging based surrogate models constructed from mesoscale computations of shock interaction with particles, *J. Comput. Phys.* **2017**, *336*, 235–260.

[68] N. K. Rai, M. J. Schmidt, H. S. Udaykumar, Collapse of elongated voids in porous energetic materials: Effects of void orientation and aspect ratio on initiation, *Phys. Rev. Fluids* **2017**, *2*, 043201.

[69] D. E. Kittell, C. D. Yarrington, J. B. Lechman, M. R. Baer, Letter: Modeling reactive shock waves in heterogeneous solids at the continuum level with stochastic differential equations, *Phys. Fluids* **2018**, *30*, 051701.

[70] A. Abdulle, W. E, B. Engquist, E. Vanden-Eijnden, The heterogeneous multiscale method, *Acta Numer.* **2012**, *21*, 1–87.

[71] W. E, B. Engquist, Z. Huang, Heterogeneous multiscale method: A general methodology for multiscale modeling, *Phys. Rev. B* **2003**, *67*, 092101.

[72] K. W. Leiter, B. C. Barnes, R. Becker, J. Knap, Accelerated scale-bridging through adaptive surrogate model evaluation, *J. Comput. Sci.* **2018**, *27*, 91–106.

[73] B. C. Barnes, K. W. Leiter, R. Becker, J. Knap, J. K. Brennan, LAMMPS integrated materials engine (LIME) for efficient automation of particle-based simulations: application to equation of state generation, *Modell. Simul. Mater. Sci. Eng.* **2017**, *25*, 055006.

[74] B. C. Barnes, C. E. Spear, K. W. Leiter, R. Becker, J. Knap, M. Lísal, J. K. Brennan. Hierarchical multiscale framework for materials modeling: Equation of state implementation and application to a Taylor anvil impact test of RDX. *Proceedings of the 19th Biennial APS Conference on Shock Compression of Condensed Matter*, **2015**.

[75] J. Knap, N. R. Barton, R. D. Hornung, A. Arsenlis, R. Becker, D. R. Jefferson, Adaptive sampling in hierarchical simulation, *Int. J. Numer. Meth. Engng.* **2008**, *76*, 572–600.

[76] P. Wurm, M. H. Ulz, A stochastic approximation approach to improve the convergence behavior of hierarchical atomistic-to-continuum multiscale models, *J. Mech. Phys. Solids* **2016**, *95*, 480–500.

[77] M. H. Ulz, Coupling the finite element method and molecular dynamics in the framework of the heterogeneous multiscale method for quasi-static isothermal problems, *J. Mech. Phys. Solids* **2015**, *74*, 1–18.

[78] M. H. Ulz, A multiscale molecular dynamics method for isothermal dynamic problems using the seamless heterogeneous multiscale method, *Comput. Methods Appl. Mech. Engrg.* **2015**, *295*, 510–524.

[79] D. Roehm, R. S. Pavel, K. Barros, B. Rouet-Leduc, A. L. McPherson, T. C. Germann, C. Junghans, Distributed Database Kriging for Adaptive Sampling, *Comput. Phys. Commun.* **2015**, *192*, 138–147.

[80] C. E. Rasmussen, C. K. I. Williams, *Gaussian processes for machine learning.* MIT Press. Cambridge, Mass., 2006.

[81] B. Rouet-Leduc, K. Barros, E. Cieren, V. Elango, C. Junghans, T. Lookman, J. Mohd-Yusof, R. S. Pavel, A. Y. Rivera, D. Roehm, A. L. McPherson, T. C. Germann, Spatial adaptive sampling in multiscale simulation, *Comput. Phys. Commun.* **2014**, *185*, 1857–1864.

[82] J. Bonet Avalos, A. D. Mackie, Dissipative particle dynamics with energy conservation, *Europhys. Lett.* **1997**, *40*, 141–146.

[83] P. Español, Dissipative particle dynamics with energy conservation, *Europhys. Lett.* **1997**, *40*, 631–636.

[84] M. Lísal, J. K. Brennan, I. V. Schweigert, M. S. Sellers, J. P. Larentzos, Dissipative Particle Dynamics with Reactions: Application to RDX Decomposition, *J. Chem. Phys.* **2019**, *151*, 114112.

[85] S. J. Plimpton, Fast Parallel Algorithms for Short-Range Molecular Dynamics, *J. Comput. Phys.* **1995**, *117*, 1–19.

[86] J. P. Larentzos, J. K. Brennan, J. D. Moore, M. Lísal, W. D. Mattson, Parallel implementation of isothermal and isoenergetic Dissipative Particle Dynamics using Shardlow-like splitting algorithms, *Comput. Phys. Commun.* **2014**, *185*, 1987–1998.

[87] T. I. Mattox, J. P. Larentzos, S. G. Moore, C. P. Stone, D. A. Ibanez, A. P. Thompson, M. Lísal, J. K. Brennan, S. J. Plimpton, Highly scalable discrete-particle simulations with novel coarse-graining: accessing the microscale, *Mol. Phys.* **2018**, *116*, 2061–2069.

[88] M. Lísal, J. K. Brennan, J. Bonet Avalos, Dissipative particle dynamics at isothermal, isobaric, isoenergetic, and isoenthalpic conditions using Shardlow-like splitting algorithms, *J. Chem. Phys.* **2011**, *135*, 204105.

[89] T. Shardlow, Splitting for Dissipative Particle Dynamics, *SIAM J. Sci. Comput.* **2003**, *24*, 1267–1282.

[90] E. Fehlberg, *Low-Order Classical Runge-Kutta Formulas with Stepsize Control and Their Application to Some Heat Transfer Problems*, TR R-315, NASA, 1969.

[91] C. P. Stone, R. L. Davis, Techniques for Solving Stiff Chemical Kinetics on Graphical Processing Units, *J. Propul. Power* **2013**, *29*, 764–773.

[92] A. Stukowski, Visualization and analysis of atomistic simulation data with OVITO-the Open Visualization Tool, *Modell. Simul. Mater. Sci. Eng.* **2010**, *18*, 015012.

[93] J. Knap, C. Spear, K. Leiter, R. Becker, D. Powell, A computational framework for scale-bridging in multi-scale simulations, *Int. J. Numer. Meth. Engng.* **2016**, *108*, 1649–1666.

[94] J. Knap, C. E. Spear, O. Borodin, K. W. Leiter, Advancing a Distributed Multi-Scale Computing Framework for Large-Scale High-Throughput Discovery in Materials Science, *Nanotechnology* **2015**, *26*, 434044.

[95] D. Groen, J. Knap, P. Neumann, D. Suleimenova, L. Veen, K. Leiter, Mastering the scales: a survey on the benefits of multiscale computing software, *Philos. Trans. R. Soc. London Ser. A* **2019**, *377*, 20180147.

[96] A. L. Nichols III, ALE-3D User's Manual, *Technical Report UCRL-MA-152204, Lawrence Livermore National Laboratory*, **2007**.

[97] T. Wang, K. Leiter, P. Plechac, J. Knap, Accelerated scale bridging with sparsely approximated Gaussian learning, *arXiv:1901.06777v1*, **2019**.

[98] M. Jette, M. Grondona. *UCRL-MA-147996: SLURM: Simple Linux Utility for Resource Management*, **2002**.

[99] L. Zhao, Z. Li, B. Caswell, J. Ouyang, G. E. Karniadakis, Active learning of constitutive relation from mesoscopic dynamics for macroscopic modeling of non-Newtonian flows, *J. Comput. Phys.* **2018**, *363*, 116–127.

[100] M. Rosenblatt, Remarks on Some Nonparametric Estimates of a Density Function, *Ann. Math. Stat.* **1956**, *27*, 832–837.

[101] E. Parzen, On Estimation of a Probability Density Function and Mode, *Ann. Math. Stat.* **1962**, *33*, 1065–1076.

[102] J. P. Larentzos, J. M. Mansell, M. Lísal, J. K. Brennan, Coarse-Grain Modelling Using an Equation-of-State Many-Body Potential: Application to Fluid Mixtures at High Temperature and High Pressure, *Mol. Phys.* **2018**, *116*, 3271–3282.

[103] I. Pagonabarraga, D. Frenkel, Non-Ideal DPD Fluids, *Mol. Simul.* **2000**, *25*, 167–175.

[104] I. Pagonabarraga, D. Frenkel, Dissipative particle dynamics for interacting systems, *J. Chem. Phys.* **2001**, *115*, 5015.

[105] P. B. Warren, Vapor-liquid coexistence in many-body dissipative particle dynamics, *Phys. Rev. E* **2003**, *68*, 066702.

[106] S. Y. Trofimov, E. L. F. Nies, M. A. J. Michels, Thermodynamic consistency in dissipative particle dynamics simulations of strongly nonideal liquids and liquid mixtures, *J. Chem. Phys.* **2002**, *117*, 9383.

[107] G. Faure, J.-B. Maillet, J. Roussel, G. Stoltz, Size consistency in smoothed dissipative particle dynamics, *Phys. Rev. E* **2016**, *94*, 043305.

[108] J. Bonet Avalos, M. Lísal, J. P. Larentzos, A. D. Mackie, J. K. Brennan, Dissipative Particle Dynamics with Energy Conservation: Density and Temperature-Dependent Potentials (in preparation), **2019**.

[109] G. Faure, J.-B. Maillet, Simulations of detonation waves with smoothed dissipative particle dynamics, *arXiv:1709.03890*, **2017**.